Carbon 132 (2018) 548–555

Contents lists available at ScienceDirect

Carbon

journal homepage: www.elsevier.com/locate/carbon

Direct nanomechanical characterization of carbon nanotube - titanium interfaces

Chenglin Yi [a], Soumendu Bagchi [b], Christopher M. Dmuchowski [a, c], Feilin Gou [a], Xiaoming Chen [d], Cheol Park [e], Huck Beng Chew [b, **], Changhong Ke [a, c, *]

[a] Department of Mechanical Engineering, State University of New York at Binghamton, Binghamton, NY 13902, USA
[b] Department of Aerospace Engineering, University of Illinois at Urbana-Champaign, Urbana, IL 61801, USA
[c] Materials Science and Engineering Program, State University of New York at Binghamton, Binghamton, NY 13902, USA
[d] Micro- and Nanotechnology Research Center, State Key Laboratory for Manufacturing Systems Engineering, Xi'an Jiaotong University, Xi'an, Shaanxi 710049, China
[e] Advanced Materials and Processing Branch, NASA Langley Research Center, Hampton, VA 23681, USA

ARTICLE INFO

Article history:
Received 24 December 2017
Received in revised form
15 February 2018
Accepted 16 February 2018
Available online 21 February 2018

Keywords:
Interfacial strength
Carbon nanotubes
Metal matrix nanocomposites
Titanium
Oxide layer

ABSTRACT

Interfacial interactions between carbon nanotubes (CNTs) and metal matrices play a critical role in the bulk mechanical properties of CNT-reinforced metal matrix nanocomposites (MMNC), but their load-transfer mechanisms remain not well understood. In this paper, we conduct single-nanotube pull-out studies with *in situ* scanning electron microscopy to quantify the mechanical strength of binding interfaces in carbon nanotube (CNT)-reinforced titanium (Ti) nanocomposites. Our nanomechanical pull-out measurements reveal a shear lag effect in the load transfer on the CNT-Ti interface. The interfacial shear strength and the maximum load-bearing capacity of the tested CNT-Ti interfaces are quantified to be about 37.8 MPa and 245 nN, respectively, both of which are substantially higher than the reported values for CNT-Al interfaces. Density functional theory calculations reveal that the experimentally observed strong CNT-Ti binding interface is attributed to strong chemisorption interactions of Ti atoms on CNT surfaces, albeit moderated by the weakening effect of the oxide layer. The research findings are useful to better understand the load transfer process on the tube-metal interface and the reinforcing mechanism of nanotubes, and ultimately contribute to the optimal design and performance of nanotube-reinforced MMNC.

1. Introduction

Nanofiber-reinforced metal matrix nanocomposites (MMNC) are lightweight materials that possess high strength and enhanced durability, and are attractive to the aerospace, automotive, and chemical industries [1–3]. The superior property enhancement in MMNC at low filler densities is attributed to the large surface-to-volume ratio of the reinforcing nanofibers, and critically relies on effective load transfer along the fiber-matrix interface [4–6]. Carbon nanotubes (CNTs) [7] are considered to be ideal reinforcements for MMNC due to their light, strong and resilient properties [8]. Among the possible metal-matrix materials, titanium (Ti) and its alloys (e.g., Titanium aluminide (TiAl)) have received the most attention [9], due to their high specific strength and corrosion resistance. Recent studies reveal substantial property enhancement in CNT-reinforced Ti MMNC. Kondoh et al. report that a 0.35 wt% CNT addition to Ti matrices results in a 28% increase in its ultimate tensile strength to 754 MPa, and a 48% increase in yield strength to 697 MPa [10]. A similar degree of yield strength enhancement (40.4% increase) is also reported by Li et al. [11], with an 11.4% increase in the ultimate tensile strength. Wang et al. also report that an addition of 0.4 wt% of CNTs resulted in a 61.5% increase in the compressive strength for Ti [12]. However, the reported mechanical properties of CNT-Ti nanocomposites still remain far from the anticipated level based on the rule of mixtures, and even underperform those of some commercially available Ti alloys (e.g., Ti-6Al-4V with a tensile strength of 900 MPa [13]). To date, direct

* Corresponding author. Department of Mechanical Engineering, State University of New York at Binghamton, Binghamton, NY 13902, USA.
** Corresponding author. Department of Aerospace Engineering, University of Illinois at Urbana-Champaign, Urbana, IL 61801, USA.
E-mail addresses: hbchew@illinois.edu (H.B. Chew), cke@binghamton.edu (C. Ke).

https://doi.org/10.1016/j.carbon.2018.02.069
0008-6223/

measurements of CNT-Ti interfacial strength necessary to understand the interfacial binding and load transfer mechanism remain unavailable [1,14]. A majority of the studies on CNT-Ti interfaces were based on bulk measurements [9,13–16] from which the interfacial properties can only be evaluated indirectly and qualitatively. For example, Munir et al. [16] attempted to evaluate the load carrying capacity of CNTs and the contribution of interfacial load transfer to the yield strength of bulk CNT-Ti composites indirectly from their measured bulk mechanical properties. The accuracy and reliability of their reported data are inevitably affected by the simplification involved in the employed theoretical model and the assumptions regarding the nanotube's complex structural morphology inside the composite matrix. The observation of microstructures in CNT-reinforced Ti MMNC by using a variety of microscopic and spectroscopic techniques also provides useful CNT-Ti interface information regarding the structural stability [9] and morphology [16] of the added CNTs inside Ti matrices and the possible reaction products on CNT-Ti interface [10,12,17,18]. However, quantitative evaluation of the CNT-Ti interfacial binding interaction and its interfacial load transfer characteristics remain elusive.

Prior studies on nanotube-reinforced polymer nanocomposites show that the tube-polymer interfacial strength is a nanomechanical signature of sophisticated tube-polymer binding interactions that depend on the chemical composition and molecular structure of the interacting tubes and polymer chains [19–22]. Similarly, the interfacial transfer mechanisms of such metal nanocomposite structures likely depend on the metal elemental composition, as well as reaction products (e.g., oxide layers) that may form along the metal-CNT interface. Therefore, the comparison of the interfacial load transfer across different tube-metal interface systems will be helpful to better understand the reinforcing mechanism. Similar to Ti, Al is a widely used metal material for aerospace and automotive industries and is also one of the most studied matrix material for CNT-reinforced MMNC. Substantial improvement in properties as a result of nanotube reinforcing has been reported. For example, 1 wt% CNT addition to Al matrix results in a 40% increase in yield strength to about 96 MPa [23]. The yield strength of a 2 wt% CNT reinforced Al nanocomposite is reported to reach about 210 MPa [24]. Nonetheless, the reported mechanical properties of CNT-Ti MMNC remain superior to those reported for CNT-Al MMNC. Noting that both Al and Ti are active materials and react spontaneously with oxygen in the air to form surface oxide layers, direct comparison between the interfacial load transfer along Al- and Ti-CNT interfaces can provide new insights on the contributing effects of the metal elemental composition and reaction products (oxide layer).

In this paper, we investigate the binding strength of CNT-Ti interfaces by using *in situ* electron microscopy single-tube pull-out techniques, and compare our results against those for CNT-Al interfaces [22]. The nanomechanical measurements capture the major failure mechanisms of CNT-Ti interfaces and enable the quantification of their load-bearing capacity and interfacial shear strength. The measurements reveal that CNT possesses a substantially stronger binding affinity with Ti as compared with Al. Density functional theory (DFT) calculations reveal that the observed strong CNT-Ti binding interface is attributed to the strong chemisorption interaction of Ti atoms on CNT surfaces, which is partially offset by the weakening effect of the oxidation layer. In comparison, the binding strength between CNT and Al is substantially enhanced by the presence of the oxide layer. To the best of our knowledge, the nanomechanical measurement presented in this paper is the *first* quantitative experimental study of the mechanical strength of CNT-Ti interfaces, and thus provides valuable insights into the load transfer mechanism in CNT-reinforced MMNC. This study also demonstrates that our *in situ* nanomechanical single-tube pull-out experimental technique is capable of characterizing the unique nanomechanical signatures of the interfaces formed by CNTs with a variety of metal matrices, which thus enables a convincing quantification and comparison of the interfacial strength across different nanotube-metal nanocomposite systems.

2. Experimental

2.1. CNT-metal nanocomposite sample preparation and characterization

Carbon nanotubes were synthesized by chemical vapor deposition methods and purchased from Sigma-Aldrich. The nanotubes were originally in the form of dry powders and were separated in deionized (DI) water using ultrasonication for two hours with the aid of ionic surfactants. Ti films were deposited at room temperature using an ATC Orion 8-E evaporator system (AJA International Inc.) with a Titanium target of 99.999% in purity (Kamis Inc.) and a base vacuum of 1×10^{-8} torr. The CNT-Ti sandwich structure was formed by first depositing a 100-nm-thick Ti film at the evaporation rate of 3 Å/s on a fresh Si substrate, followed by spin coating depositions of a well-dispersed nanotube solution (about 0.1% in CNT concentration) at a speed of 800 rpm for one minute and then the deposition of another Ti film of 100 nm in thickness on top under the same conditions. The acceleration voltage of the electron gun was fixed at 7 kV and the temperature inside the vacuum chamber during deposition was just slightly higher than room temperature per the instrument manufacturer. The sandwiched CNT-Ti nanocomposite films were fractured by means of cracking the substrate using a diamond scriber, and some of the embedded tubes protruded as straight free-standing cantilever structures. The AFM characterization of the dispersed tubes and the deposited Ti films was performed inside an NTEGRA AFM (NT-MDT) that operates in tapping mode at ambient environment. Transmission electron microscopy (TEM) characterization of the CNT-Ti nanocomposite films with protruding tubes was performed using a JEM 2100F TEM (JEOL Ltd.). Ellipsometry characterization of Ti films was performed using a UVISEL spectroscopic ellipsometer from Horiba.

2.2. In situ single-tube nanomechanical pull-out measurements

The *in situ* nanomechanical single-tube pull-out measurements were performed inside an FEI Nanolab 600 dual-beam electron microscope. Silicon AFM probes (model CSG 01, NT-MDT) were employed as the force sensors in the pull-out tests. The spring constant of each employed AFM probe was calibrated using thermal tuning methods and was found to be within the range of 0.04–0.09 N/m. The AFM probe was mounted to a 3D piezo stage that possesses 1 nm displacement resolution in the X-Y-Z axes [25–28] and was controlled to move at a rate of approximately 0.5–1 μm/s. The embedded tube length was measured directly using the high-resolution electron beam with a resolution of a few nanometers. The pull-out load was calculated based on the spring constant of the AFM force sensor and its last recorded deflection in the pull-out test with a resolution of about 0.5–1.0 nN.

3. Results and discussion

3.1. In situ electron microscopy nanomechanical single-tube pull-out measurements

Fig. 1(a) illustrates the employed *in situ* electron microscopy nanomechanical single-tube pull-out technique, in which the tested CNT-Ti interface is formed inside a sandwiched metal/CNT/

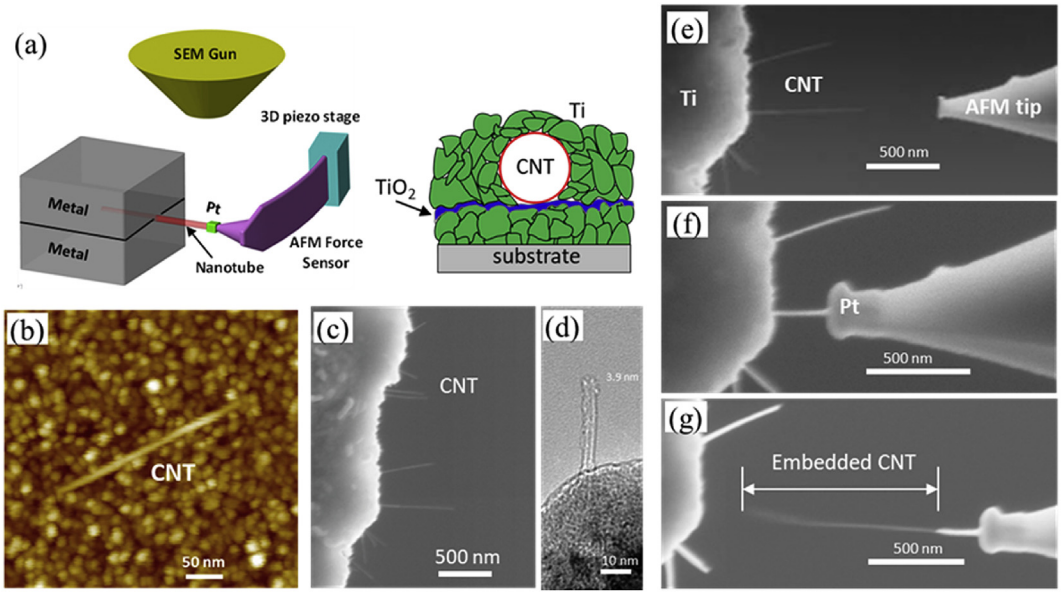

Fig. 1. **(a)** Schematics of the *in situ* nanomechanical single-tube pull-out testing technique inside a high-resolution scanning electron microscope (*left*) and the cross-sectional Ti/CNT/Ti sandwiched thin-film nanocomposite (*right*). The drawings are not to scale. (**b**) AFM image of one CNT on the surface of an electron-beam deposited Ti film. (**c**) A fractured CNT-Ti thin-film nanocomposite that shows protruding CNTs. (**d**) TEM image of one protruding CNT of 3.9 nm in outer diameter from a Ti matrix. (**e**)–(**g**) Selected SEM snapshots that show the key processes in one representative single-tube pull-out measurement: **(e)** An AFM tip was controlled to approach and then touch the free end of one selected protruding CNT that was oriented perpendicular to the AFM cantilever back surface; **(f)** The free end of the protruding tube was spot-welded to the AFM tip by means of EBID of Pt; **(g)** The embedded portion of the tube was completely pulled out of the metal matrix by applying a tensile force. (A colour version of this figure can be viewed online.)

metal thin-film nanocomposite. The detailed working principle and experimental setup of this nanomechanical testing technique have been documented in prior reports [19–22] and are only briefly described here. A pre-calibrated atomic force microscopy (AFM) cantilever acts as a force sensor and is mounted vertically to the stage of a 3D piezo nanomanipulator. The pull-out measurements are performed inside a high-resolution scanning electron microscope (FEI Nanolab 600 electron microscope). The free end of a selected protruding CNT cantilever is first attached to the tip of the AFM probe with the aid of electron beam induced deposition (EBID) of Pt. The AFM cantilever is then displaced to apply an increasing tensile force until the embedded tube segment is fully stretched out of the composite film. The entire nanomanipulation operation is monitored by using high-resolution electron beams with a few nanometer spatial resolutions.

The employed double-walled carbon nanotubes (DWCNTs) were dispersed in deionized water by means of ultrasonication with the aid of surfactants, and their lengths were controlled to be mostly below 2 μm through controlling the ultrasonication time [29]. AFM studies show that the tube diameter is polydispersed. The median tube diameter is found to be about 3.1 nm, and >90% of the tubes have diameters within the range of 2.0–4.2 nm. The Ti film was deposited at room temperature using electron beam evaporation methods (See Experimental section for details). Fig. 1(b) shows an AFM image of one CNT of about 3.3 nm in diameter and 318 nm in length on the surface of an e-beam deposited Ti film. The grain size of the e-beam evaporated Ti films was measured from the recorded AFM images and was found to be on average about 28 nm. Spectroscopic ellipsometry measurements show a 5 nm oxide layer formed on the Ti film surface after the deposition of CNT solutions because Ti is an active material and reacts spontaneously with contact of air and/or water. Because the subsequent Ti deposition was performed in a high vacuum environment, the oxide layer was not expected to appear at the contact between CNTs and the second deposited Ti film. Fig. 1(c) shows one of the fractured sandwiched CNT-Ti thin-film nanocomposites with several protruding nanostructures. Transmission electron microscopy (TEM) inspection, as exemplified by the image shown in Fig. 1(d), confirms that those protruded structures are individual CNTs with clean surfaces that are free of metal residues. Due to the small wall number and diameter of the employed tubes as well as the relatively large thickness of the deposited metal films, the tube-metal interface could not be readily observed by using TEM.

Fig. 1(e)-(g) show three selected SEM snapshots of one representative single-tube pull-out measurement on a partially embedded CNT with a protruding length of 772 nm. The pull-out of the nanotube was observed to occur as a catastrophic failure of the CNT-metal interface when the stretching force reached a certain value (i.e., pull-out force). For this measurement, the pull-out force and the embedded tube length are measured to be about 242 nN and 1.19 μm, respectively.

Interface failure scenarios other than the successful single-tube pull-out as the one shown in Fig. 1(g) were also observed and were categorized as tube fracture and telescopic pull-out, which are

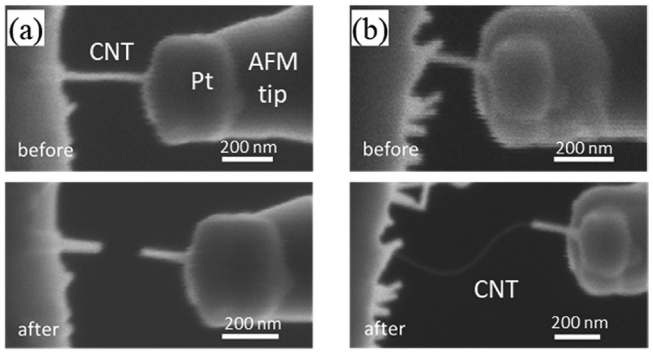

Fig. 2. Selected SEM snapshots showing the two types of failure scenarios observed during the nanomechanical pull-out measurements: (a) fracture of a nanotube; (b) telescopic pull-out of a nanotube.

exemplified by the selected SEM snapshots shown in Fig. 2(a)–(b), respectively. It is noted that the observed fracture of the tube occurred in the protruding tube segment, while the telescopic pull-out occurred as a result of the breaking of the outermost shell of the nanotube followed by subsequent pull-out of the inner tube shells. Both tube fracture and telescopic pull-out are clear signs of effective load transfer in nanofiber-reinforced nanocomposites [30]. These tube failure scenarios were identified from the recorded SEM images, and are excluded from mechanical strength analysis of the CNT-metal interface.

Fig. 3 shows a summary of the pull-out measurements from 21 independent successful single-tube pull-out tests, with embedded nanotube lengths ranging from about 87 nm to 2.41 μm. It is observed that the pull-out force first increases linearly with the embedded length before reaching a force plateau, which is a clear sign of the shear lag effect. This shear lag effect is one of the major energy dissipation mechanisms in nanofiber-reinforced nanocomposites. It is noted that similar shear-lag phenomena were reported on the pull-out measurements of nanotube-polymer interfaces [19–21] as well as recent studies of CNT-Al interfaces [22]. In particular, prior measurements on CNT-Al interfaces [22] were performed using the same sample preparation and testing schemes as shown in Fig. 1, and also using the same batch of dispersed CNTs as employed in the present study. The usage of the same methodology and materials in these two nanomechanical studies enables a meaningful and convincing comparison of the interfacial binding interactions of CNTs with Ti versus with Al, which is exhibited in Fig. 3. The key sample parameters and the measured/calculated interfacial properties for these two types of CNT-metal samples are summarized in Table 1.

By assuming the tested CNTs in both studies follow the same probability distribution in diameter, the data displayed in Fig. 3 clearly show that CNT possesses a statistically stronger binding affinity with Ti as compared with Al. The maximum load-bearing capacity of the CNT-Ti interface, which is calculated as the average value of the force plateau, is found to be 245 ± 8 nN and is about 13% higher than that of the CNT-Al interface (217 ± 8 nN). The average interfacial shear strength (IFSS) of the CNT-Ti interface τ_{ave}, is quantified based on the data points in the initial linearly increasing segment and is given as $\tau_{ave} = \frac{P}{\pi \times D \times l}$, in which P is the pull-out force, D is the diameter of the tube, l is the embedded tube length. In our experiments, the diameters of the tested tubes could not be measured precisely as they approach the resolution limit of the electron beam. Here we evaluate the IFSS based on the measured median tube diameter (i.e., $D = 3.1$ nm), which is deemed as the most representative value for the CNT-metal interfacial strength. The IFSS of the CNT-Ti interface is calculated to be 37.8 ± 9.3 MPa, and is about 32% higher than that of the CNT-Al interface (28.7 ± 3.4 MPa) as displayed in Fig. 3, and is about 52% higher than the value 24.8 ± 3.2 (MPa) reported by Kawasaki and co-workers [31]. The critical tube embedded length [22] is quantified as the junction value in the bilinear fitting curve and is found to be about 735 nm for the CNT-Ti interface as compared with about 780 nm for the CNT-Al interface. It is noted that ~28 nm Ti grains in the tested CNT-Ti thin-film nanocomposites are several orders of magnitude smaller than the ~10 μm or larger grains in bulk CNT-reinforced Ti composites reported previously [10–12]. The stronger CNT-Ti interface reported here could be favorably impacted by the finer metal grains [32].

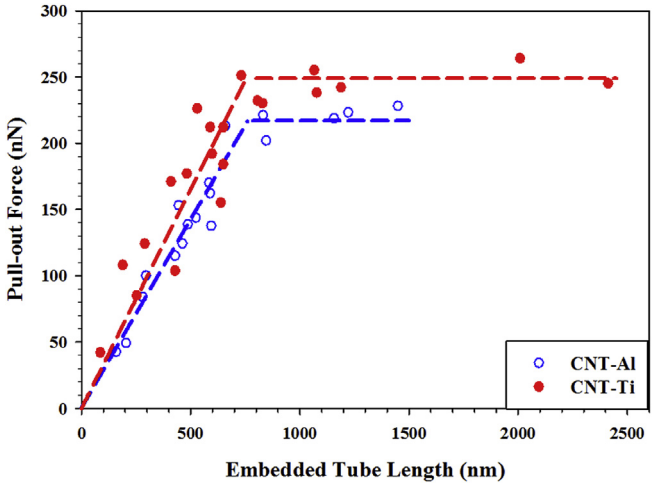

Fig. 3. The measured dependence of the pull-out force on the embedded tube length for CNT-Ti interfaces (red solid dots), which is contrasted with the measurement data reported on CNT-Al interfaces (blue empty dots, reproduced from Ref. [22]). The dashed lines are the bilinear fitting curves to the respective data sets. (A colour version of this figure can be viewed online.)

3.2. Quantification of the interfacial load transfer on CNT-Ti interfaces

In this section, we analyze the interfacial load transfer on the tube-metal interface using a continuum mechanics model that takes into account the yielding of the metal layer in direct binding contact with nanotube surfaces. Due to the shear lag effect, the interfacial shear stress on the nanotube-metal interface has a non-uniform distribution. The interfacial shear stress possesses its maximum value at the tube entry position, and then decays rapidly towards the tube's embedded end position. The shear stress decay rate is inversely correlated to the Young's modulus of the matrix material [33]. It is noted that pure titanium reportedly possesses a yield stress (in tension) of about 400 MPa [34] and a corresponding yield shear stress of about 231 MPa, the latter of which is significantly higher than the calculated average IFSS (37.8 MPa). However, due to the non-uniform distribution of the interfacial shear stress and its high decay rate as a result of Ti's high Young's modulus (116 GPa), it is possible that Ti metal grains in the vicinity of the binding interface, in particular those at or close to the tube entry position, may yield under the pull-out load, which is confirmed by our theoretical analysis.

The continuum mechanics model is illustrated by the insert diagram in Fig. 4. For simplicity, a homogeneous interface between CNT and Ti along the entire embedded tube length is assumed. The deformation of the metal matrix caused by the interfacial shear stress is assumed to be pure shear and to occur only within a thin metal layer that is in direct binding contact with the CNT surface [22,36], which is marked as the shaded area in the illustration drawing in Fig. 4. It is noted that the whole metal matrix (including the interfacial metal layer) is assumed to be free of initial internal stress. This assumption is justified by the fact that the Ti films in our studies were deposited using electron beam vacuum evaporation techniques and the vacuum chamber temperature was just slightly above room temperature, both of which help to minimize the process/thermal-induced internal stress in the deposited Ti films [37].

The equilibrium equation for the embedded tube segment is given as

$$\sigma_z \cdot \pi D^2 + 4 \int_{z_0}^{z} \tau_i \pi \cdot D dz = 0, \quad (1)$$

where z is the coordinate axis along the tube length with z_0 as the

Table 1
Summary of the key sample parameters and the experimentally measured and calculated interface properties for CNT-Ti interfaces (this study) and CNT-Al interfaces (data reproduced from Ref. [22]).

	Nanotubes type and outer diameter	Metal preparation approach, total thickness, and average grain size	Maximum pull-out load (nN)	Critical embedded length (nm)	Average interfacial shear stress (MPa)
CNT-Al interface (ref. [22])	Double-walled; 2–4.2 nm (3.1 nm median value)	e-beam evaporation, 200 nm, about 35 nm	217 ± 8	780	28.7 ± 3.4
CNT-Ti interface (this work)	Double-walled; 2–4.2 nm (3.1 nm median value)	e-beam evaporation, 200 nm, about 28 nm	245 ± 8	735	37.8 ± 9.3

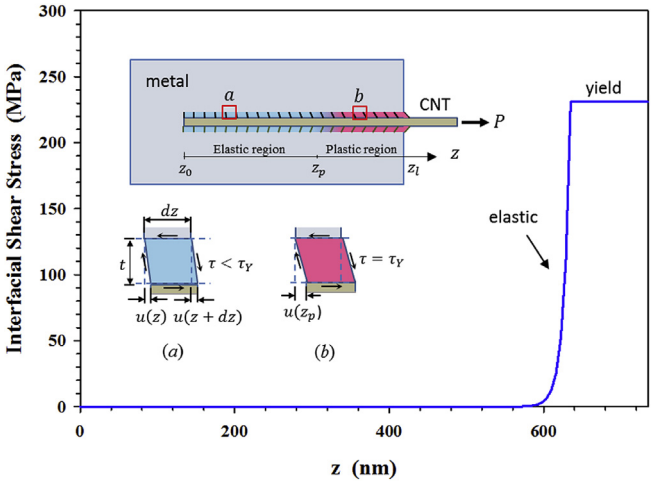

Fig. 4. Theoretically predicted interfacial shear stress distribution for a CNT-Ti interface with an embedded tube length of 735 nm. The insert diagram is a schematic illustration of the shear lag model and interfacial shear stress on the CNT-metal interface. The shaded region represents an interfacial metal layer and its deformation is visualized with the aid of the added short mesh lines and two representative free-body diagrams for elements in the elastic and plastic regions, respectively. (A colour version of this figure can be viewed online.)

position of the tube end. σ_z is the normal stress in the tube and is given as $\sigma_z = E_f\frac{du(z)}{dz}$, in which E_f is the Young's modulus of the nanotube and $u(z)$ is the displacement of the tube; τ_i is the interfacial shear stress. Here, Ti is assumed as a linearly elastic and perfectly plastic material with a Young's modulus E_m, a Poisson's ratio ν_m and a yield shear stress τ_Y. The interfacial shear stress in the elastic deformation region ($z_0 \le z < z_P$) and the plastic deformation (yield) region ($z_P \le z \le l$) of the interfacial metal layer with a thickness of t is given as

$$\tau_i = \begin{cases} \dfrac{E_m}{2(1+\nu_m)\cdot t}\cdot u(z), & z_0 \le z < z_P \\ \tau_Y, & z_P \le z \le l \end{cases} \quad (2)$$

The equilibrium equation for the embedded tube segment is given as

$$D\cdot E_f\frac{d^2u(z)}{dz^2} + 4\frac{E_m}{2(1+\nu_m)\cdot t}u(z) = 0, \quad z_0 \le z < z_P \quad (3a)$$

$$D\cdot E_f\frac{d^2u(z)}{dz^2} + 4\tau_Y = 0, \quad z_P \le z \le l \quad (3b)$$

The boundary conditions used in the model include $\sigma_z = 0$ at $z = z_0$ and $\tau_i = \tau_Y$ at $z = z_P$. The summation of the interfacial shear force along the entire tube-metal interface equals the pull-out load, i.e., $\int_{z_0}^{l} \tau_i\pi\cdot Ddz = P$. It is noted that the thickness of the interfacial metal layer (t) is obtained through fitting the experimentally measured values of the pull-out force and the tube embedded length as presented in Fig. 3. Equations (3a)–(3b) are solved numerically with the following parameters: $E_m = 116$ GPa, $\tau_Y = 231$ MPa, and $\nu_m = 0.32$ for titanium [38]; $E_f = 1$ TPa and $D = 3.1$ nm for CNTs.

Fig. 4 shows a theoretically predicted interfacial shear stress profile for a CNT-Ti interface with an embedded tube length of 735 nm and a pull-out load of 245 nN. The calculation of the theoretical curve is based on a fitting parameter t of 5.3 nm. The plot shows that substantial yield deformations occur in the interfacial metal layer when the pull-out event occurs even though the average IFSS of the nanotube-metal interface is far below the yield shear stress of the metal matrix. It is also displayed in the plot that the elastic deformation region has a quite steep decay in shear stress for z within the range of 550 nm–635 nm. The observed rapid decay in shear stress is ascribed to the high Young's modulus of titanium. The results shown in Fig. 4 indicate that the maximum interfacial shear stress on the tube-metal interface can reach or even exceed the original yield shear stress of the work-hardening metal material, which was also recently demonstrated in the single-tube pull-out study of the CNT-Al interface [22]. Therefore, it is essential to take into account the plastic deformation of the metal grains in the neighboring of the tube-metal interface in the continuum mechanics modeling of the single-tube pull-out measurements.

3.3. Quantification of the CNT-metal binding interaction using DFT calculations

To better understand the above-mentioned experimental findings, we perform DFT calculations by using Vienna Ab initio Simulation Package (VASP) to quantify the interfacial binding characteristics between CNTs and Ti/Al metal matrices. We adopt the Vanderbilt ultra-soft pseudo potentials for calculating the interaction between the ionic core electrons and the valence electrons, and use the Perdew–Burke–Ernzehof (PBE) form of the generalized gradient approximation (GGA) or the Ceperly-Alder (CA) form of the local density approximation (LDA) for exchange and correlation. For the purpose of our interfacial studies, we treat CNTs as equivalent planar graphene sheets. Our periodic monoclinic supercells, as shown in Fig. 5 (a–i) and 5 (a-ii), are composed of repeated 6-atomic-layer-thick slabs of Al (111) and Ti (0001), each placed 2.5 Å above the graphene sheets. The respective metal-graphene model structures have initial lattice mismatch strains of ~1.1% and 4.3%, which are calculated with respect to the graphene lattice. A 12–15 Å vacuum layer is also introduced at the top of each supercell to expose only one side of the graphene sheet to the metal substrate. We adopt a plane wave basis energy cutoff of 450 eV, and use a gamma centered 5 × 5 × 1 Monkhorst-Pack k-point sampling scheme for Brillouin zone sampling. The supercells are then quantum-mechanically relaxed to their minimum energy positions using the conjugate gradient method with a force tolerance criterion of 0.001 eV/Å. Using the LDA (GGA) approximation, we obtain lattice spacing of 3.97 (4.00) Å within the Al crystal, with C-C bond

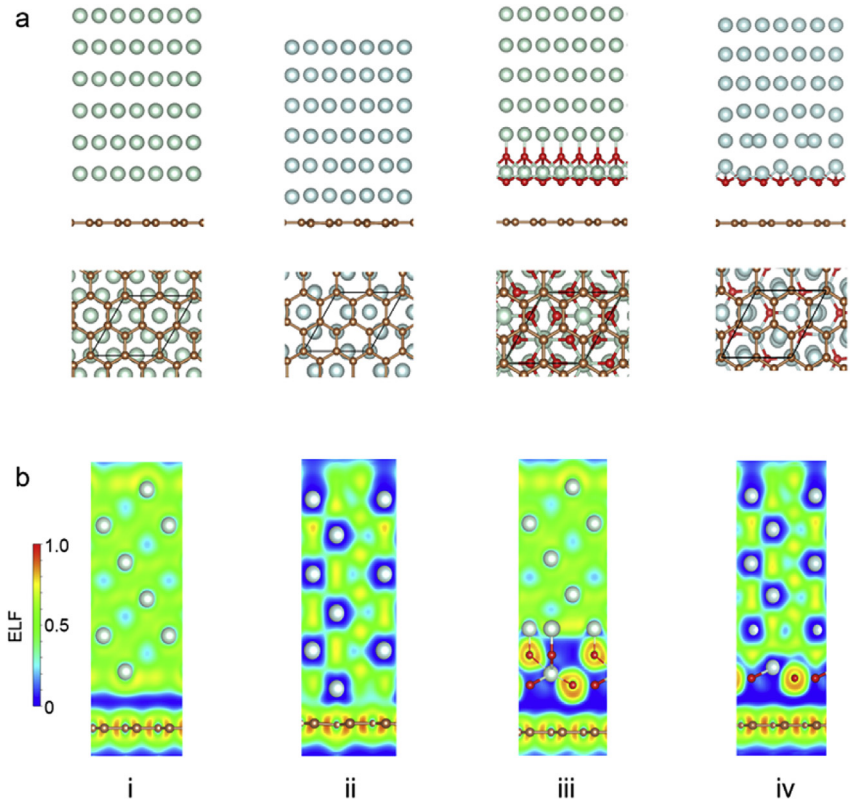

Fig. 5. First principle calculations of the interfacial bonding properties between Al/Ti metal substrates and graphene. (a) Side view and bottom view atomic configurations of Al (111) (i) and Ti (0001) (ii) substrates, and surface-oxidized Al (111) (iii) and Ti (0001) (iv) substrates, attached to graphene sheet; black outline in bottom view denotes size of each periodic supercell. Ti or Al atoms are colored in grey, C atoms in orange, and O atoms in red. (b) Electron localized function (ELF) contours of the metal-graphene systems that correspond to (a). (A colour version of this figure can be viewed online.)

distance of 1.40 (1.42) Å for the attached graphene sheet; for the Ti crystal, we obtain lattice spacing of 2.85 (2.89) Å, with C-C bond distance of 1.44 (1.45) Å for the attached graphene sheet.

Our DFT calculations show that graphene-Al (111) has an interfacial separation distance of 3.16 (3.67) Å as compared to 2.16 (2.20) Å for graphene-Ti (0001), based on the LDA (GGA) approximation; these interfacial separation distances suggest that graphene is physisorbed on Al (111), but is chemisorbed on Ti (0001). We calculate the metal-graphene binding energy, E_b, by subtracting the energies of free-standing graphene and the isolated metal slab from that of the combined metal-graphene system, and normalizing the difference with respect to the interfacial area. With this definition, more negative E_b indicates stronger cohesive bonding across the interface. The graphene-Al interface has E_b of $-0.57\,eV/nm^2$ and $-0.46\,eV/nm^2$ from LDA and GGA calculations, versus $-15.82\,eV/nm^2$ (LDA) and $-10.90\,eV/nm^2$ (GGA) for the graphene-Ti interface. The higher cohesive energy across the graphene-Ti interface is in qualitative agreement with the experimental findings; however, the order-of-magnitude difference in cohesive energy from DFT calculations does not coincide well with the level of difference in experimentally measured IFSS. We attribute this discrepancy to the presence of oxide layers formed on both the exposed Ti and Al surfaces during the deposition of CNTs. We repeat our DFT calculations for graphene attached to surface-oxidized Al and Ti slabs, as shown in Fig. 5 (a-iii) and 5 (a-iv); these surface-oxide layers were created by positioning O atoms at the most stable adsorption sites on the close-packed Al and Ti surfaces, which are the face-centered cubic and face-centered cubic/hexagonal-close-packed sites, respectively [39,40]. In the presence of the oxidized surface layer, the cohesive energy for graphene-Ti-O is found to reduce dramatically to $E_b = -0.85\,eV/nm^2$ (LDA) and $-0.04\,eV/nm^2$ (GGA), but the cohesive energy for graphene-Al-O is increased to $E_b = -2.21\,eV/nm^2$ (LDA) and $-0.847\,eV/nm^2$ (GGA) which is about three-fold higher than that for graphene-Ti-O. The corresponding interfacial separation distances are now 2.95 (3.23) Å and 3.00 (3.31) Å for graphene-Al-O and graphene-Ti-O, respectively, based on the LDA (GGA) approximation, which indicate that the graphene sheets are now physisorbed on both the surface-oxidized metal substrates. The finding that the oxide layer increases the binding interaction in CNT-Al interface also supports our recent experimental observation that thermal annealing results in a substantially stronger CNT-Al interface [22].

To obtain a general overview of the atomic interactions, we examine the electron localized function (ELF) contours as viewed along a cross-sectional cut across all four graphene-metal systems in Fig. 5(b) using the GGA approximation. The ELF is a measure of the probability of finding an electron near another electron with the same spin [41]. Qualitatively, a large ELF close to 1 (red) corresponds to a region with a high probability of finding electron localization as in covalent bonding, whereas an ELF close to 0.5 (green) corresponds to a region of electron gas-like behavior as in metallic bonding. An intermediate ELF value of 0.75 (yellow) can be interpreted as corresponding to ionic bonding. For the graphene-Al structure displayed in Fig. 5 (b–i), we observe an abrupt change from metallic bonding within the pure Al slab to covalent bonding within graphene with the absence of appreciable bonding across the interface (dark blue region with ELF <0.1). In contrast, ELF between graphene and pure Ti displayed in Fig. 5(b-ii) is distinctly higher (~0.3), which confirms that graphene is chemically bonded

to Ti. This stronger binding interaction of graphene to Ti versus Al has been attributed to the hybridization of the unoccupied *d*-orbitals in transition metals such as Ti with the *2p*-orbitals of C atoms in graphene [42–45]. For the surface-oxidized graphene-Al-O structure shown in Fig. 5(b-iii), bonding between O and Al atoms is now distinctly ionic. Close examination shows localization of electron pockets closer to the graphene sheet, which results in stronger interfacial binding compared to pure graphene-Al systems. The transition in ELF contours across the interface for graphene-Ti-O in Fig. 5(b-iv) is quite similar to that for graphene-Al-O. Clearly, the ionically bonded O atoms, which now reside above the graphene π-cloud, weaken any possible Ti-C interaction. The DFT findings indicate that it is plausible to tune the mechanical strength of CNT-metal interfaces through purposely engineered oxide layers, which can be accomplished by using facile manufacturing processes, such as thermal annealing [22]. To enhance the interfacial strength and overall bulk properties of CNT-Ti MMNC, the composite manufacturing is preferably conducted in oxygen-free environments, such as vacuum or inert gas environments. In contrast, the exposure of the Al matrix material to the ambient environment to form aluminum oxide can significantly enhance the binding strength of the CNT-Al interface.

4. Conclusion

In summary, the load-bearing capacity and interfacial shear strength of CNT-Ti interfaces are characterized by using *in situ* electron microscopy single-tube pull-out techniques in conjunction with DFT calculations. The nanomechanical measurements reveal the shear lag effect on the CNT-Ti interface and show a 32% higher interfacial shear strength compared to CNT-Al interface. DFT calculations reveal that the strong CNT-Ti binding interface is due to the chemisorption of Ti atoms on CNT surfaces, compared to the physisorption of Al atoms on CNT. However, the presence of oxide layers on the metal surface is found to enhance the mechanical strength of CNT-Al interfaces, but to weaken CNT-Ti interfaces. These research findings help to better understand the load transfer process on the tube-metal interface and the reinforcing mechanism of nanotubes, and ultimately contribute to the optimal design and performance of nanotube-reinforced MMNC.

Acknowledgements

This work was supported by United States Air Force Office of Scientific Research - Low Density Materials program under Grant No FA9550-15-1-0491, and by the National Science Foundation under Grant Nos. CMMI-1537333, CMMI-1429176 (CK) and CMMI-1538162 (HBC). We thank Dr. In-Tae Bae for his assistance with the TEM characterization and Dr. Anju Sharma for her assistance with the ellipsometry characterization. C.M.D acknowledges fellowship support from the New York NASA Space Grant Consortium. The DFT calculations were performed using the computational resources provided by TACC (Award No. TG-MSS130007) and the Blue Waters sustained-petascale computing project which is supported by the National Science Foundation (Award Nos. OCI-0725070 and ACI-1238993) and the State of Illinois, USA.

References

[1] S.R. Bakshi, D. Lahiri, A. Agarwal, Carbon nanotube reinforced metal matrix composites - a review, Int. Mater. Rev. 55 (2013) 41, https://doi.org/10.1179/095066009X12572530170543.
[2] M. Haghshenas, Metal–Matrix Composites, Reference Module in Materials Science and Materials Engineering, Elsevier, 2016, https://doi.org/10.1016/B978-0-12-803581-8.03950-3.
[3] F. Banhart, Interactions between metals and carbon nanotubes: at the interface between old and new materials, Nanoscale 1 (2009) 201–213, https://doi.org/10.1039/B9NR00127A.
[4] M.L. Minus, H.G. Chae, S. Kumar, Single wall carbon nanotube templated oriented crystallization of poly(vinyl alcohol), Polymer 47 (2006) 3705–3710, https://doi.org/10.1016/j.polymer.2006.03.076.
[5] Y. Zhang, K. Song, J. Meng, M.L. Minus, Tailoring polyacrylonitrile interfacial morphological structure by crystallization in the presence of single-wall carbon nanotubes, ACS Appl. Mater. Interfaces 5 (2013) 807–814, https://doi.org/10.1021/am302382m.
[6] X. Tao, L. Dong, X. Wang, W. Zhang, B.J. Nelson, X. Li, B4C-Nanowires/Carbon-Microfiber hybrid structures and composites from cotton t-shirts, Adv. Mater. 22 (2010) 2055–2059, https://doi.org/10.1002/adma.200903071.
[7] S. Iijima, Helical microtubules of graphitic carbon, Nature 354 (1991) 56–58, https://doi.org/10.1038/354056a0.
[8] M.S. Dresselhaus, Carbon Nanotubes, Springer, Berlin, 2001.
[9] T. Kuzumaki, O. Ujiie, H. Ichinose, K. Ito, Mechanical characteristics and preparation of carbon nanotube fiber-reinforced Ti composite, Adv. Eng. Mater. 2 (2000) 416–418, https://doi.org/10.1002/1527-2648(200007)2:7<416:AID-ADEM416>3.0.CO;2-Y.
[10] K. Kondoh, T. Threrujirapapong, H. Imai, J. Umeda, B. Fugetsu, Characteristics of powder metallurgy pure titanium matrix composite reinforced with multi-wall carbon nanotubes, Compos. Sci. Technol. 69 (2009) 1077–1081, https://doi.org/10.1016/j.compscitech.2009.01.026.
[11] S. Li, B. Sun, H. Imai, T. Mimoto, K. Kondoh, Powder metallurgy titanium metal matrix composites reinforced with carbon nanotubes and graphite, Compos. Appl. Sci. Manuf. 48 (2013) 57–66, https://doi.org/10.1016/j.compositesa.2012.12.005.
[12] F.-C. Wang, Z.-H. Zhang, Y.-J. Sun, Y. Liu, Z.-Y. Hu, H. Wang, A.V. Korznikov, E. Korznikova, Z.-F. Liu, S. Osamu, Rapid and low temperature spark plasma sintering synthesis of novel carbon nanotube reinforced titanium matrix composites, Carbon 95 (2015) 396–407, https://doi.org/10.1016/j.carbon.2015.08.061.
[13] G. Welsch, R. Boyer, E.W. Collings, Materials properties handbook: titanium alloys, ASM International, 1994, ISBN 978-0871704818.
[14] A. Azarniya, M.S. Safavi, S. Sovizi, A. Azarniya, B. Chen, H.R. Madaah Hosseini, S. Ramakrishna, Metallurgical challenges in carbon nanotube-reinforced metal matrix nanocomposites, Metals 7 (2017) 384, https://doi.org/10.3390/met7100384.
[15] K.S. Munir, Y. Li, D. Liang, M. Qian, W. Xu, C. Wen, Effect of dispersion method on the deterioration, interfacial interactions and re-agglomeration of carbon nanotubes in titanium metal matrix composites, Mater. Des. 88 (2015) 138–148, https://doi.org/10.1016/j.matdes.2015.08.112.
[16] K.S. Munir, Y. Zheng, D. Zhang, J. Lin, Y. Li, C. Wen, Microstructure and mechanical properties of carbon nanotubes reinforced titanium matrix composites fabricated via spark plasma sintering, Mater. Sci. Eng. 688 (2017) 505–523, https://doi.org/10.1016/j.msea.2017.02.019.
[17] T. Taguchi, H. Yamamoto, S. Shamoto, Synthesis and characterization of single-phase TiC nanotubes, TiC nanowires, and carbon nanotubes equipped with TiC nanoparticles, J. Phys. Chem. C 111 (2007) 18888–18891, https://doi.org/10.1021/jp0756909.
[18] A. Felten, I. Suarez-Martinez, X. Ke, G. Van Tendeloo, J. Ghijsen, J.-J. Pireaux, W. Drube, C. Bittencourt, C.P. Ewels, The role of oxygen at the interface between titanium and carbon nanotubes, ChemPhysChem 10 (2009) 1799–1804, https://doi.org/10.1002/cphc.200900193.
[19] X. Chen, M. Zheng, C. Park, C. Ke, Direct measurements of the mechanical strength of carbon nanotube–poly(methyl methacrylate) interfaces, Small 9 (2013) 3345–3351, https://doi.org/10.1002/smll.201202771.
[20] X. Chen, L. Zhang, M. Zheng, C. Park, X. Wang, C. Ke, Quantitative nanomechanical characterization of the van der Waals interfaces between carbon nanotubes and epoxy, Carbon 82 (2015) 214–228, https://doi.org/10.1016/j.carbon.2014.10.065.
[21] X. Chen, L. Zhang, C. Park, C.C. Fay, X. Wang, C. Ke, Mechanical strength of boron nitride nanotube-polymer interfaces, Appl. Phys. Lett. 107 (2015) 253105, https://doi.org/10.1063/1.4936755.
[22] C. Yi, X. Chen, F. Gou, C.M. Dmuchowski, A. Sharma, C. Park, C. Ke, Direct measurements of the mechanical strength of carbon nanotube - aluminum interfaces, Carbon 125 (2017) 93–102, https://doi.org/10.1016/j.carbon.2017.09.020.
[23] B. Boesl, D. Lahiri, S. Behdad, A. Agarwal, Direct observation of carbon nanotube induced strengthening in aluminum composite via in situ tensile tests, Carbon 69 (2014) 79–85, https://doi.org/10.1016/j.carbon.2013.11.061.
[24] X. Liu, C. Li, J. Eckert, K.G. Prashanth, O. Renk, L. Teng, Y. Liu, R. Bao, J. Tao, T. Shen, J. Yi, Microstructure evolution and mechanical properties of carbon nanotubes reinforced Al matrix composites, Mater. Char. 133 (2017) 122–132, https://doi.org/10.1016/j.matchar.2017.09.036.
[25] C.H. Ke, N. Pugno, B. Peng, H.D. Espinosa, Experiments and modeling of carbon nanotube-based NEMS devices, J. Mech. Phys. Solid. 53 (2005) 1314–1333, https://doi.org/10.1016/j.jmps.2005.01.007.
[26] C.H. Ke, H.D. Espinosa, In situ electron microscopy electromechanical characterization of a bistable NEMS device, Small 2 (2006) 1484–1489, https://doi.org/10.1002/smll.200600271.
[27] C. Ke, M. Zheng, G. Zhou, W. Cui, N. Pugno, R.N. Miles, Mechanical peeling of free-standing single-walled carbon nanotube bundles, Small 6 (2010) 438–445, https://doi.org/10.1002/smll.200901807.
[28] M. Zheng, C. Ke, Elastic deformation of carbon-nanotube nanorings, Small 6

(2010) 1647–1655, https://doi.org/10.1002/smll.201000337.
[29] H.B. Chew, M.-W. Moon, K.R. Lee, K.-S. Kim, Compressive dynamic scission of carbon nanotubes under sonication: fracture by atomic ejection, Proceedings of the Royal Society of London A: Mathematical, Physical and Engineering Sciences (2010), https://doi.org/10.1098/rspa.2010.0495 rspa20100495.
[30] K. Lau, Interfacial bonding characteristics of nanotube/polymer composites, Chem. Phys. Lett. 370 (2003) 399–405, https://doi.org/10.1016/S0009-2614(03)00100-3.
[31] W. Zhou, G. Yamamoto, Y. Fan, H. Kwon, T. Hashida, A. Kawasaki, In-situ characterization of interfacial shear strength in multi-walled carbon nanotube reinforced aluminum matrix composites, Carbon 106 (2016) 37–47, https://doi.org/10.1016/j.carbon.2016.05.015.
[32] C.F. Deng, D.Z. Wang, X.X. Zhang, A.B. Li, Processing and properties of carbon nanotubes reinforced aluminum composites, Mater. Sci. Eng. 444 (2007) 138–145, https://doi.org/10.1016/j.msea.2006.08.057.
[33] K.R. Jiang, L.S. Penn, Improved analysis and experimental evaluation of the single filament pull-out test, Compos. Sci. Technol. 45 (1992) 89–103, https://doi.org/10.1016/0266-3538(92)90031-W.
[34] J. Magargee, F. Morestin, J. Cao, Characterization of flow stress for commercially pure titanium subjected to electrically assisted deformation, J. Eng. Mater. Technol. 135 (2013) 041003–041003-10, https://doi.org/10.1115/1.4024394.
[36] S. Mahesh, J.C. Hanan, E. Üstündag, I.J. Beyerlein, Shear-lag model for a single fiber metal matrix composite with an elasto-plastic matrix and a slipping interface, Int. J. Solid Struct. 41 (2004) 4197–4218, https://doi.org/10.1016/j.ijsolstr.2004.02.050.
[37] H. Garbacz, P. Wieciński, B. Adamczyk-Cieślak, J. Mizera, K.J. Kurzydłowski, Studies of aluminium coatings deposited by vacuum evaporation and magnetron sputtering, J. Microsc. 237 (2010) 475–480, https://doi.org/10.1111/j.1365-2818.2009.03297.x.
[38] H. Gercek, Poisson's ratio values for rocks, Int. J. Rock Mech. Min. Sci. 44 (2007) 1–13, https://doi.org/10.1016/j.ijrmms.2006.04.011.
[39] F. Libisch, C. Huang, P. Liao, M. Pavone, E.A. Carter, Origin of the energy barrier to chemical reactions of O2 on Al(111): evidence for charge transfer, not spin selection, Phys. Rev. Lett. 109 (2012) 198303, https://doi.org/10.1103/PhysRevLett.109.198303.
[40] S.-Y. Liu, F.-H. Wang, Y.-S. Zhou, J.-X. Shang, Ab initio study of oxygen adsorption on the Ti(0001) surface, J. Phys. Condens. Matter 19 (2007) 226004, https://doi.org/10.1088/0953-8984/19/22/226004.
[41] B. Silvi, A. Savin, Classification of chemical bonds based on topological analysis of electron localization functions, Nature 371 (1994) 683–686, https://doi.org/10.1038/371683a0.
[42] P.A. Khomyakov, G. Giovannetti, P.C. Rusu, G. Brocks, J. van den Brink, P.J. Kelly, First-principles study of the interaction and charge transfer between graphene and metals, Phys. Rev. B 79 (2009) 195425, https://doi.org/10.1103/PhysRevB.79.195425.
[43] A. Maiti, A. Ricca, Metal-nanotube interactions - binding energies and wetting properties, Chem. Phys. Lett. 395 (2004) 7–11, https://doi.org/10.1016/j.cplett.2004.07.024.
[44] C. Rohmann, Q. Sun, D.J. Searles, Interaction of Al, Ti, and Cu atoms with boron nitride nanotubes: a computational investigation, J. Phys. Chem. C 120 (2016) 3509–3518, https://doi.org/10.1021/acs.jpcc.5b10698.
[45] C.-K. Yang, J. Zhao, J.P. Lu, Binding energies and electronic structures of adsorbed titanium chains on carbon nanotubes, Phys. Rev. B 66 (2002) 041403, https://doi.org/10.1103/PhysRevB.66.041403.